

Article

A methodology for gas flaring detection and characterisation using SLSTR

Alexandre Caseiro ^{1,*} , Gernot Rücker ², Joachim Tiemann ², David Leimbach ², Eckehard Lorenz ³, Olaf Frauenberger ⁴, and Johannes W. Kaiser ¹

¹ Max Planck Institute for Chemistry, Mainz, Germany

² Zebris GbR, Munich, Germany

³ DLR, Berlin, Germany

⁴ DLR, Neusterlitz, Germany

* Correspondence: alexandre.caseiro@mpic.de; Tel.: +49-6131-305-4071

Abstract: Gas flaring is a disposal process widely used in the oil extraction and processing industry. It consists in the burning of unwanted gas at the tip of a stack. We have successfully adapted the VIIRS Nightfire algorithm for the detection and characterisation of gas flares to SLSTR observations on-board the Sentinel-3 satellites. A hot event at temperatures typical of a gas flare will produce a local maximum in the night-time readings of the shortwave and mid-infrared (SWIR and MIR) channels of SLSTR. The SWIR band centered at 1.61 μm is closest to the expected spectral radiance maximum and serves as the primary detection band. The hot source is characterised in terms of temperature and area by fitting the sum of two Planck curves, one for the hot source and another for the background, to the radiances from all the available SWIR, MIR and thermal infra-red channels of SLSTR. The flaring radiative power is calculated from the gas flare temperature and area. Our algorithm differs from the original VIIRS Nightfire algorithm in three key aspects: (1) It uses a granule-based contextual thresholding to detect hot pixels, being independent of the number of hot sources present and their intensity. (2) It analyses entire clusters of hot source detections instead of individual pixels. This is arguably a more comprehensive use of the available information. (3) The co-registration errors between hot source clusters in the different spectral bands are calculated and corrected. This also contributes to the SLSTR instrument validation. Cross-comparisons of the new gas flare characterisation with temporally close observations by the higher resolution German FireBIRD TET-1 small satellite and with the Nightfire product based on VIIRS on-board the Suomi-NPP satellite show general agreement for an individual flaring site in Siberia and for several flaring regions around the world. Small systematic differences to VIIRS Nightfire are nevertheless apparent. The retrieved flaring radiative power can be used to calculate flared gas volumes when calibrated against reported flared gas volumes. The estimated flared gas volume can be further combined with published emission factors in order to compute emissions of atmospheric trace constituents like carbon dioxide and black carbon.

Keywords: Gas flaring; SLSTR

1. Introduction

Gas flaring (GF) is part of the upstream oil and gas industry processes as a means of disposing of unwanted natural gas through high temperature oxidation at the tip of a stack. Flaring produces greenhouse gases (GHG) and black carbon as the main by-products of the combustion. In terms of the global GHG budget, the importance of flaring is diminutive [1]. However, regarding the short-lived climate forcer black carbon, GF may be of regional prime importance. GF has been identified as the main input of black carbon in boreal regions [2,3], with implications for the albedo of snow-covered surfaces, the earth's radiative balance [4,5] and the Arctic amplification phenomenon [6], being therefore of global relevance [7]. Again in the Arctic region, GF's contribution to the NO_2

concentrations is important, and has been increasing in the past decade [8]. GF also impacts the local environment [9]: noise [10,11], a visual pollution [12,13], heat stress [12,14] and the emission of further air pollutants like polycyclic aromatic hydrocarbons, volatile organic compounds and acid rain precursors [15–18].

The information on flared volumes and emissions is sparse and methodologically inconsistent due to technical difficulties and the lenient reporting requirements and guidelines of some jurisdictions. Remote sensing offers the possibility of a globally consistent and independent monitoring of flaring. The identification of flaring in the night-time data of visible and near infra-red (Vis-NIR) spectral range [19,20] allowed for the first semi-automatic monitoring of flares from space [21–23]. With the advent of vegetation fire detection products based on mid and thermal infrared bands (MIR and TIR), flaring was highlighted as a main source of false alarms [24,25]. This feature was exploited to study flaring [26,27] and later the additional evaluation of short-wave infrared (SWIR) bands allowed for a more accurate detection [28–32], being at present the state-of-the-art.

Casadio *et al.* [29] considered the radiances at four wavelengths (in the SWIR, MIR and TIR bands of (A)ATSR) to be a linear combination of black body radiances from two areas with different temperatures within the satellite pixel footprint (actively flaming and background). Elvidge *et al.* [30] developed the Nightfire algorithm in which a Planck curve is fitted to the night-time Vis-IR measurements of the Visible Infrared Imaging Radiometer Suite instrument (VIIRS, on-board the Suomi-National Polar Partnership) and considered an emission scaling factor to estimate the flare size. The latter methodology was further developed into a dual Planck curve fitting (one Planck curve fitted to the background signal and one fitted to the flare signal) to the observations in five bands (NIR, SWIR and MIR) of VIIRS [32] and used to retrieve information on the global distribution and characteristics of gas flaring. Its results are made public by NOAA's National Centre for Environmental Information as daily global fields.

The BIRD algorithm was developed to apply the bi-spectral method [33] to MIR and TIR data from the Hot Spot Recognition System (HSRS) instrument on board the bi-spectral Infrared Detection (BIRD) Experimental Small Satellite (2001–04) [34–36]. It was designed to retrieve effective temperature, effective area and effective radiative power of sub-pixel hot sources, namely fires [37,38]. The methodology was later ported to the successor FireBIRD mission, with a similar sensor in IR and a modified Vis-NIR payload on board of the TET-1 (Technologieerprobungsträger-1) spacecraft [39].

The burnt gas volume in billion cubic metres (BCM) and emissions to the atmosphere can be estimated from satellite observations of gas flaring. This estimation uses a conversion factor that scales observed radiative energy release to BCM together with emission factors that convert BCM into the amount of different chemical smoke species. The emission factors have been measured in-situ and reported in the literature. The conversion factor has been calculated as fraction of reported BCM and the observed radiative energy in entire countries. [32].

The Sea and Land Surface Temperature Radiometer (SLSTR) instrument on board ESA's Sentinel-3 features night-time observations in two SWIR (S5: 1.61 μm and S6: 2.25 μm), one MIR (S7: 3.74 μm) and two TIR bands (S8: 10.85 μm and S9: 12.0 μm). The instrument also measures in two fire-dedicated bands (F1: 3.74 μm and F2: 10.85 μm) with the same central wavelength and band width as S7 and S8, but extended dynamical ranges to prevent saturation over active fires. [40] The distribution of the SLSTR spectral channels with SWIR, MIR and 2 channels in TIR should allow for the detection and characterisation of GF via the SWIR detection and the dual Planck curve fitting methodologies. A dedicated SLSTR gas flare product would nicely fill some of the observation gaps of the VIIRS Nightfire product since the instruments are on satellites with different overpass times. Furthermore, the long-term commitment of the EU Copernicus programme, which funds the Sentinel satellites, would warrant data availability well into the 2030s.

In this paper, we present a new algorithm for gas flare detection and characterization from SLSTR observations and apply it to actual SLSTR data. Section 2 presents the data used. Section 3 describes the developed methodology in detail. In Section 4 we present the results of the application of the

Table 1. Comparison between the used sensors.

	HSRS on TET-1	VIIRS on Suomi-NPP	SLSTR on Sentinel-3A
Start of operation	2013	2011	2016
Orbit altitude (km)	Sun synchronous 445	Sun synchronous 834	Sun synchronous 814.5
SWIR bands (μm)		I3: 1.58 – 1.64 M11: 2.225 – 2.275	S5: 1.58 – 1.65 S6: 2.23 – 2.28
Infrared bands (μm)	MIR: 3.40 – 4.20 TIR: 8.50 – 9.30	I4: 3.55 – 3.93 M13: 3.97 – 4.13 I5: 10.50 – 12.40	S7, F1: 3.55 – 3.93 S8: 10.40 – 11.30 S9, F2: 11.50 – 12.50
Ground resolution (m)	IR-bands: 170	I-bands: 375 M-bands: 750	S4–S6: 500 S7–S9, F1–F2: 1000
Swath (km)	IR: 178	3040	1420

newly developed algorithm at the regional level in four regions of interest (West Africa, The North and Caspian Seas and the Persian Gulf) and evaluate our methodology against the VIIRS Nightfire product. The performance of our algorithm is further evaluated against VIIRS Nightfire and retrievals based on HSRS on-board the German small satellite TET-1 at the level of a single gas flaring site on the Yamal peninsula, Northern Siberia. Finally, in Section 5 we present our conclusions.

2. Data

SLSTR Level 1b version 2 products obtained from the ESA's Sentinel Expert User's Hub in January 2017 were used for this work. The downloaded products were selected using a geographic criterion (four regions of interest: West Africa, the Caspian and the North Seas and the Persian Gulf) and a time of day criteria (only night-time acquisitions). The products were sampled in the second half of 2016. For the SWIR bands (S5 and S6), the data available in the product are top of the atmosphere (TOA) radiances, while for the MIR (S7 and F1) and TIR (S8, S9 and F2) bands, the available data are brightness temperatures. The latter were converted back to TOA radiances using lookup tables provided by the European Space Agency.

FireBird TET-1 level-2 co-registered data of TET-1 night time acquisition mode (only MIR and TIR bands at 170 m spatial resolution) were obtained for near coincident or temporally close SLSTR and TET-1 observations during polar night conditions in 2016/17 over the Yamal peninsula and other areas in Northern Siberia. Due to solar light contamination, only data North of about 70° latitude could be used, which excluded the other regions. Probably due to the extremely cold background, the standard level-2 fire processor of FireBird [39] failed to identify valid background pixels, and thus did not detect any hot clusters. The co-registered data were therefore reprocessed with the BIRD night-time algorithm [38] which was adapted to the spatial resolution of TET-1 and the cold background. The algorithm for fire detection and characterisation output includes an estimate of the fire area and its uncertainty, the fire temperature and its uncertainty, and the fire radiative power [38] which were used for comparison with the temporally close SLSTR retrievals.

VIIRS Nightfire data [30] were downloaded from the NOAA website (https://ngdc.noaa.gov/eog/viirs/download_viirs_fire.html). No further processing was applied to this dataset.

Table 1 summarizes the specifications of the used sensors, while Table 2 summarizes the data used.

3. Methodology

A general flowchart of the developed methodology is shown in Figure 1. The individual processing steps are described in the following sections.

Table 2. Data used in this study. The number of VIIRS products was derived from the VIIRS Nightfire dataset from NOAA, corresponding to the products which exhibited detections co-located in space and time.

	Sensor	Region	Sampling dates	n
Regional study	SLSTR	North Sea	17/11 – 18/12/2016	189
		Caspian Sea	17/11 – 20/12/2016	99
		Persian Gulf	17/11 – 31/12/2016	153
		West Africa	25/07 – 29/09/2016	364
	VIIRS (Nightfire)	Global	2016	587
Single site study	SLSTR	Yamal peninsula	15/12/2016	43
	VIIRS (Nightfire)		–	6
	HSRS		02/01/2017	12

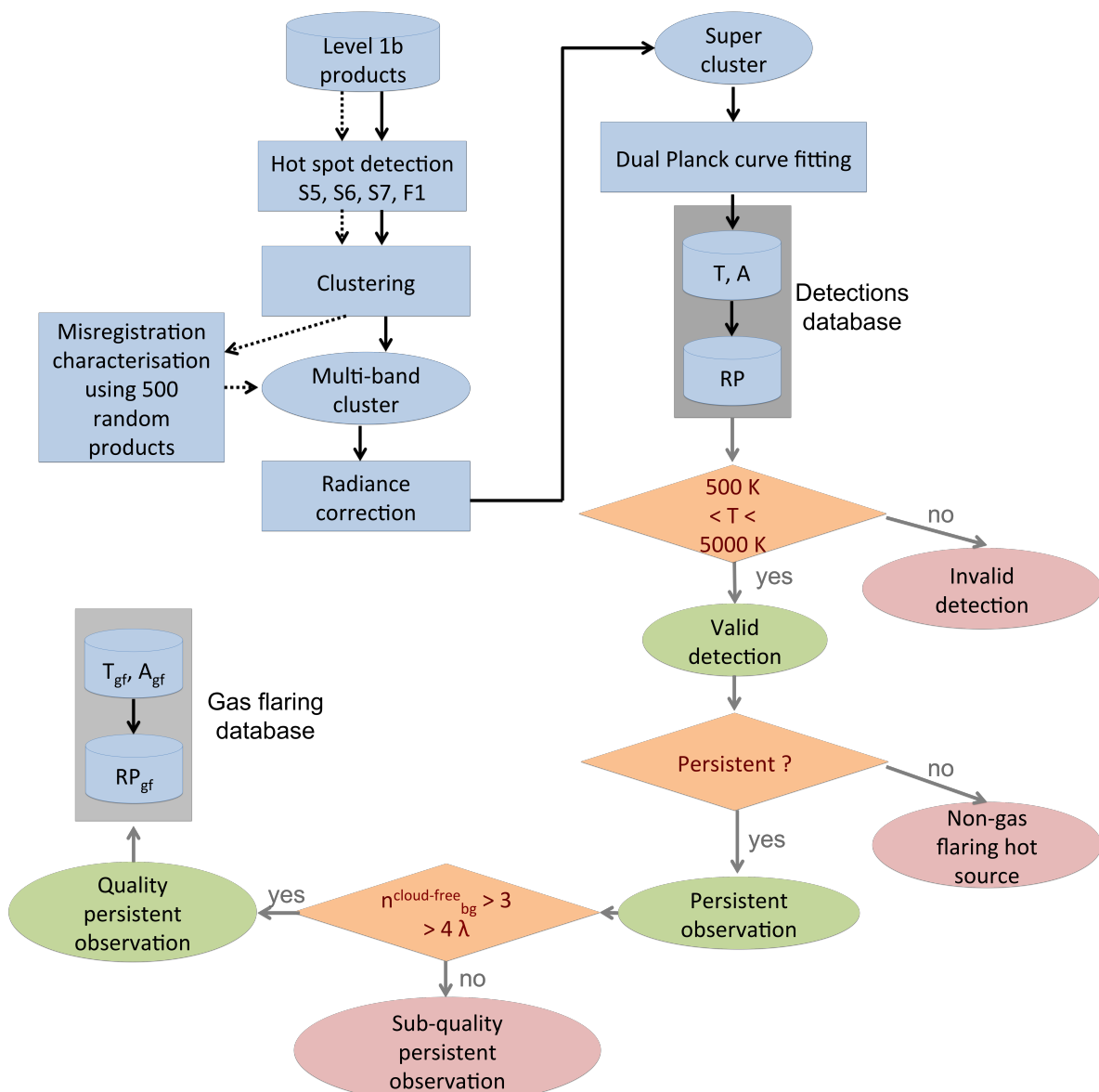


Figure 1. General algorithm flowchart for the detection of gas flares and their characterisation: temperature (T), area (A) and radiative power (RP). The dotted line represents the one-time misregistration determination. The parameterization was then used when building the multi-band cluster. $n_{bg}^{cloud-free} > 3$ represents at least three cloud-free pixels in the background. $> 4\lambda$ means there is radiance data at least 4 of the 5 wavelengths considered by the algorithm.

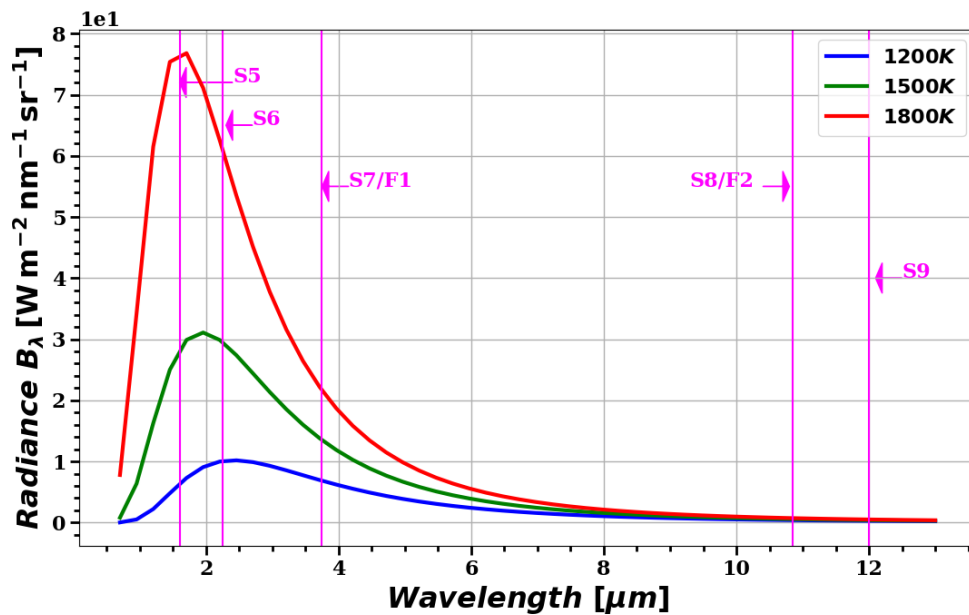


Figure 2. Planck curves for typical gas flaring temperatures and SLSTR SWIR (S5 and S6), MIR (S7 and F1) and TIR (S8, S9 and F2) channels.

3.1. Detection

The SLSTR SWIR channels S5 and S6 capture the peak radiation of typical gas flaring temperatures around 1500 K as given by the Planck equation (Figure 2). Remote detection of gas flares with space-borne SWIR observations has been using *a priori* fixed thresholds on one or several bands [28,29,31] or determining the threshold based on the pixel's surroundings, i.e. contextual thresholding [30,32,41].

In the present work, we use contextual thresholding by identifying all pixels that stand out of the continuum of background values by more than one digitization step size of the respective satellite band. All pixels with a radiance larger or equal to the threshold radiance $B_{\lambda}^{threshold}$ are detections and processed further:

$$B_{\lambda}^{threshold} = \min\{B_{\lambda,i}^{largest} | B_{\lambda,i}^{largest} - B_{\lambda,i-1}^{largest} > sf_{\lambda}\} \quad (1)$$

where $B_{\lambda}^{largest} = \{B_{\lambda,-999}, \dots, B_{\lambda,0} | B_{\lambda,i} \leq B_{\lambda,i+1}\}$ is the ordered set of the 1000 largest radiances in the granule (typically SWIR bands: 2400×3000 pixels per granule, MIR and TIR bands: 1200×1500 pixels per granule), and sf_{λ} is the scale factor for the product and that band, which is calculated from the smallest interval between records due to the digitization of the analogue radiometric signal.

Several approaches were tested, the selected one was the most robust, identifying hot pixels in different contexts. This approach captures hot pixels when there is a gradual or an abrupt increase (upper and lower plots of Figure 3, respectively). While not fixed, and therefore adaptable to product-specific conditions, this contextual methodology is not statistical and therefore not directly sensitive to the number of hot events sampled and their intensity.

At the end of this step, a collection of i hot pixels are registered, for each of the four SWIR and MIR bands, with the following information:

- hot pixel location (x_i, y_i) as pixel index pair
- radiance $B_{\lambda,i}$ in $Wm^{-2}\mu m^{-1}sr^{-1}$
- area $A_{\lambda,i}$ in m^2 .

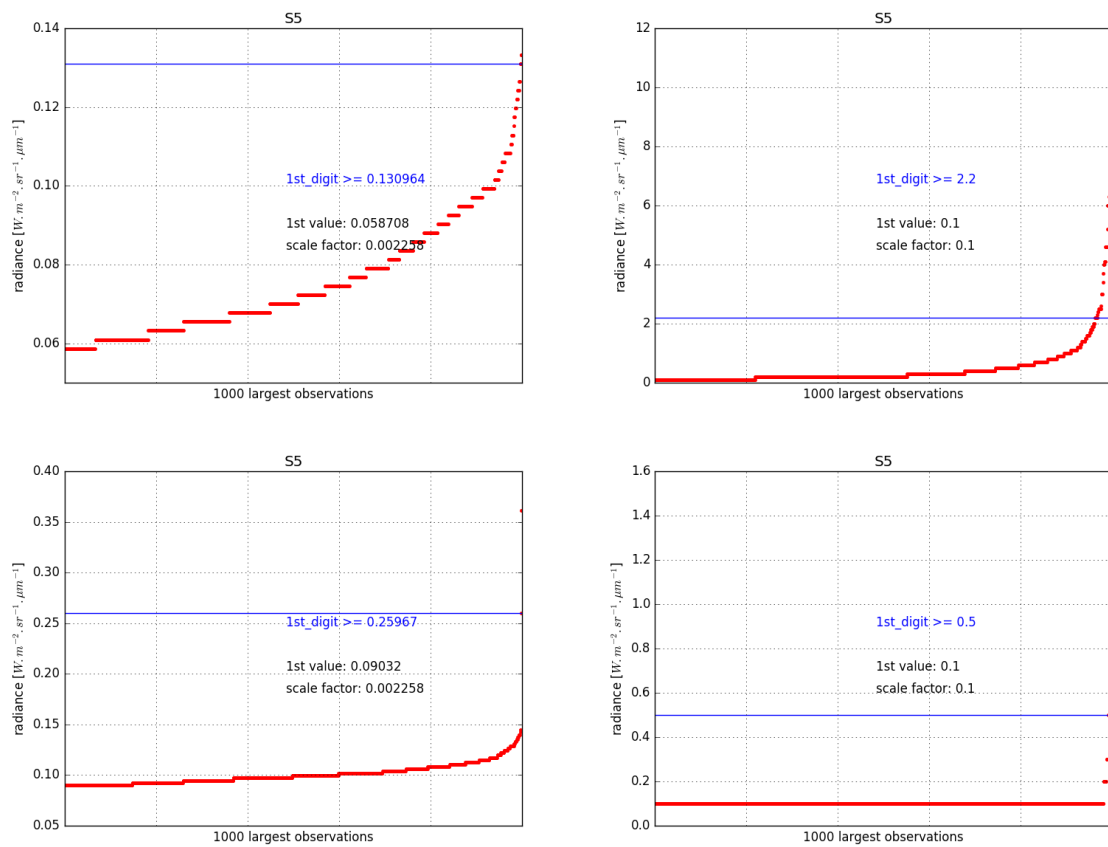


Figure 3. Four examples of thresholding for the S5 band. The horizontal line marks the threshold value. The threshold is set contextually as the lowest radiance value whose difference to the closest inferior radiance value is larger than the scale factor.

3.2. Clustering

The clustering of contiguous hot pixels is necessary because the signal of a single gas flare may influence more than one pixel [27,42]. It may also be the case that a single gas flare is detected in two or more adjacent pixels. [31,41] Indeed, a flaring facility may comprise arrays of many flares with sizes of up to several hundred metres, while individual stations are several kilometres apart.

A cluster is defined as a set of hot pixels which are adjacent spacially. A cluster may comprise only one pixel if none of its adjacent pixels are hot.

A background area is defined as extending two pixels beyond the cluster's limits in any direction, including diagonally. For each single pixel i of the n cluster's pixels, the radiance $B_{\lambda,i}$ and area $A_{\lambda,i}$ are registered. Likewise, for each single pixel j of the m background pixels, $B_{\lambda,j}$ and $A_{\lambda,j}$ are registered.

For each cluster, the following quantities are then computed:
the average radiance in [$Wm^{-2}\mu m^{-1}sr^{-1}$]:

$$B_{\lambda} = \frac{\sum_{i=1}^n B_{\lambda,i}}{n} \quad (2)$$

the average background radiance in [$Wm^{-2}\mu m^{-1}sr^{-1}$]:

$$B_{\lambda}^{bg} = \frac{\sum_{j=1}^m B_{\lambda,j}}{m} \quad (3)$$

the background radiance standard deviation in [$Wm^{-2}\mu m^{-1}sr^{-1}$]:

$$\sigma_{\lambda}^{bg} = \frac{1}{m} \sum_{j=1}^m (B_{\lambda,j} - B_{\lambda}^{bg})^2 \quad (4)$$

the cluster area in [m^2]:

$$A_{\lambda} = \sum_{i=1}^n A_{\lambda,i} \quad (5)$$

the cluster x-position as across-track index:

$$x_{\lambda} = \frac{\sum_{i=1}^n x_{\lambda,i} \times B_{\lambda,i}}{\sum_{i=1}^n B_{\lambda,i}} \quad (6)$$

the cluster y-position as along-track index:

$$y_{\lambda} = \frac{\sum_{i=1}^n y_{\lambda,i} \times B_{\lambda,i}}{\sum_{i=1}^n B_{\lambda,i}} \quad (7)$$

where n is the number of hot pixels in the cluster and m is the number of pixels in the hot cluster's background.

3.3. Misregistration characterisation

A hot event at temperatures typical of a gas flare will produce a local maximum in the SWIR and MIR channels (see Figure 2), which will be translated into a cluster in those bands. The MIR fire channel

F7 of SLSTR has been designed with a different footprint size and position than the corresponding SWIR channels. Because of these differences the clusters in the different bands cannot be spatially superimposed.

The S5 cluster location is used as reference because it is the band closest to the maximum energy output expected for a gas flare (Figure 2). The along-track and across-track distances between a cluster in the reference SWIR band S5 and the closest cluster in the remaining SWIR and MIR bands (S6, S7 and F1) are being parameterised as functions of the across-track position using second order polynomials. Its parameters are determined by fitting 500 random products from the dataset. The confidence intervals for the distances are assumed to be bound by second order polynomials that are vertically shifted such that 10% of the data points are below, resp. above (Figure 4).

3.4. Misregistration correction: building multi-band clusters

Multi-band clusters $C^{flaring}$ are subsequently constructed. They consist of the single-band clusters C_λ with λ in S5, S6, S7 and F1 that observe the same hot source. The SWIR cluster C_{S5} is used as reference. Then those cluster from the remaining bands (C_λ with λ in S6, S7 and F1) that are closest to after correction of the misregistration are added. In doing so, only clusters in the confidence intervals are considered:

$$\min\{d|(x_\lambda^{min} \leq |x_{S5} - x_\lambda| \leq x_\lambda^{max} \wedge y_\lambda^{min} \leq |y_{S5} - y_\lambda| \leq y_\lambda^{max})\} \rightarrow C_\lambda^{flaring} = C_\lambda \quad (8)$$

where

C_λ is any of the λ -band clusters (λ in S6, S7 and F1),

$C_\lambda^{flaring}$ is the λ -band cluster within the multi-band cluster $C^{flaring}$ (λ in S6, S7 and F1),

$d = ((x_\lambda - x_\lambda^{avg})^2 + (y_\lambda - y_\lambda^{avg})^2)^{\frac{1}{2}}$ is the distance between C_λ and the parameterised misregistration position for the band λ ,

x_{S5} and y_{S5} are the across track and along track position of the S5 reference cluster $C_{S5}^{flaring}$,

x_λ and y_λ are the across track and along track position of C_λ ,

x_λ^{avg} , x_λ^{min} and x_λ^{max} are the average, minimum and maximum distances in the across track axis given by the misregistration parameterisation as a function of the reference cluster across track position x_{S5} ,

y_λ^{avg} , y_λ^{min} and y_λ^{max} are the average, minimum and maximum distances in the along track axis given by the misregistration parameterisation as a function of the reference cluster across track position y_{S5} .

For the TIR bands S8, S9 and F2, the flaring high-temperature event is not expected to impact the radiance (Figure 2). The average radiance for each TIR band 2 pixels around the reference S5 cluster position is then associated to the multi-band cluster.

3.5. Radiance corrections

The SWIR radiances in S5 and S6 exhibit a systematic overestimation of 11 and 20%, respectively. [43] Following recommendations by ESA, all values in the SWIR bands were corrected accordingly. This correction needs to be verified and possibly updated for future versions of SLSTR products.

After building the multi-band clusters, the MIR S7 channel is checked for saturation. If the S7 radiance is above the saturation value ($0.56 \text{ Wm}^{-2}\mu\text{m}^{-1}\text{sr}^{-1}$, corresponding to a brightness temperature of 306K) in any of the hot pixels within the cluster, then it is discarded. If the S7 cluster is discarded or not present, the F1 cluster is used. The F1 band is a fire dedicated channel of SLSTR which measures at the same wavelength as the S7 channel, but with a larger dynamic range and lower sensitivity. Only F1 clusters where all of the pixels have a brightness temperature within the linearity range 300–480K are considered. This way, sensitivity is maximized without compromising detection.

3.6. Super Cluster definition

The areas of the individual clusters in the SWIR and MIR bands within a multi-band cluster may vary. To overcome this, hypothetical super clusters, with perfect coregistration and identical footprint

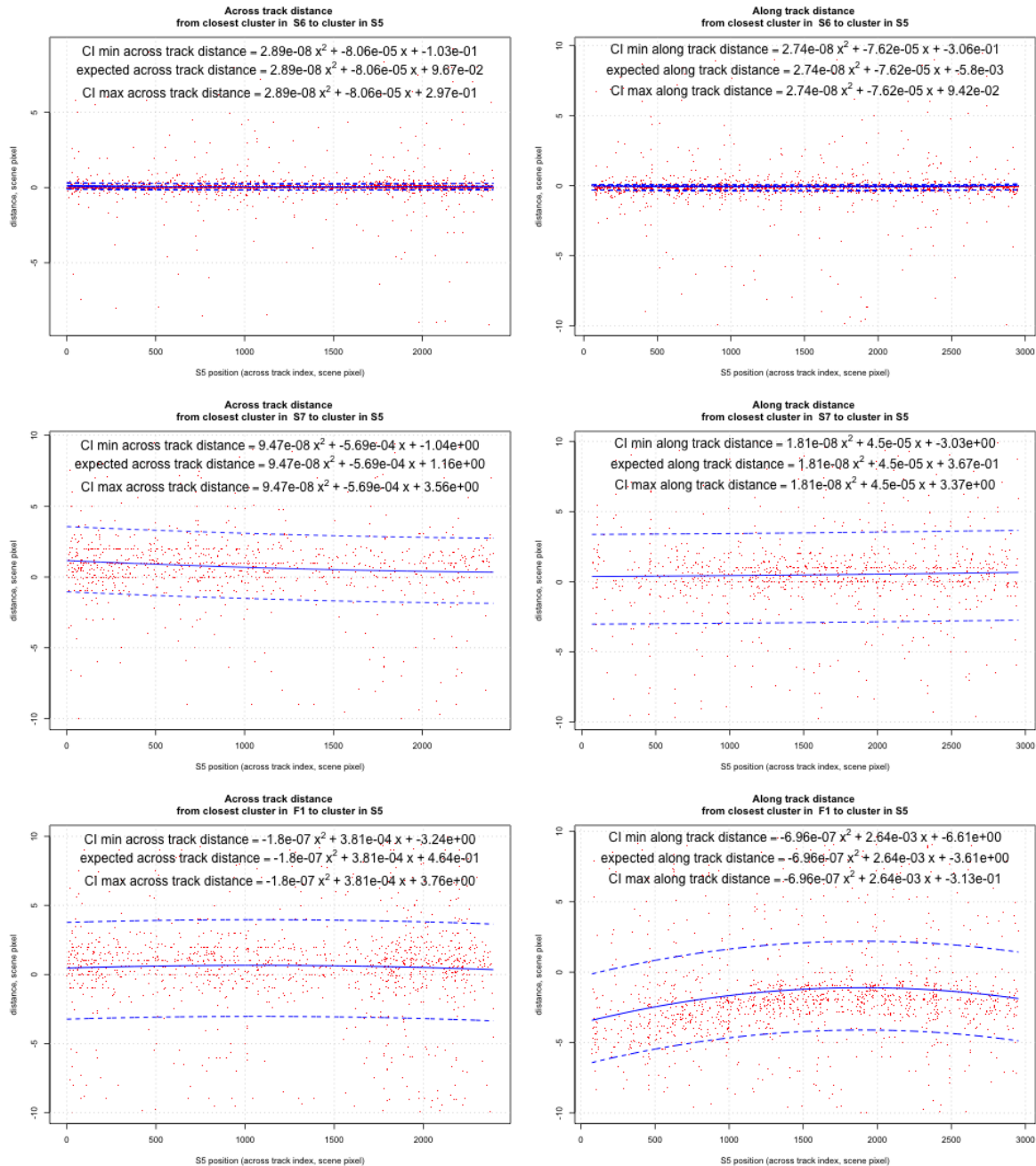


Figure 4. Parameterizations of the distances between a cluster in S5 and the closest cluster in S6, S7 and F1 as a function of the scan index. The solid line shows the best fit (second order polynomial). The dashed lines are parallel to the best fit so that 10% of the points are above resp. below. They represent the confidence interval.

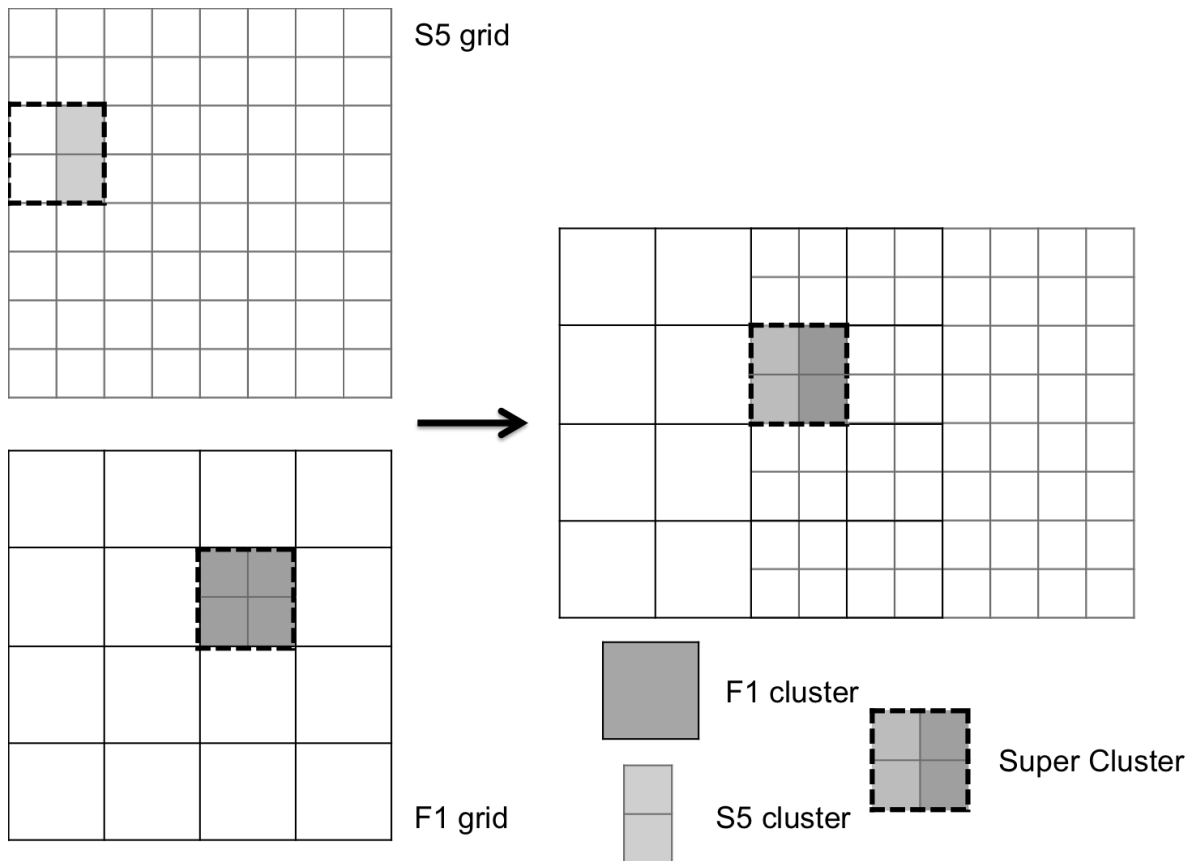


Figure 5. Super cluster creation.

areas in all bands, are built. The largest of the individual band clusters' areas A_λ is chosen as area $A_{cluster}$ of the super cluster (Figure 5).

For each band's cluster $C_\lambda^{flaring}$ within a multi-band cluster $C^{flaring}$, the observed cluster radiance B_λ^{obs} is calculated as area-weighted average of the observed radiances of the cluster and the background:

$$B_\lambda^{obs} = \frac{B_\lambda \times A_\lambda + B_\lambda^{bg} \times (A_{cluster} - A_\lambda)}{A_{cluster}} \quad (9)$$

It is assumed that the background radiance B_λ^{bg} is constant in the vicinity of the cluster. For the TIR bands (S8, S9 and F2) the weighting is not necessary and the average registered radiance is used.

3.7. Planck curve fitting

In order to determine the temperature and the area of the flaring event, the sum of two Planck curves is fitted to the radiance data of the multiband cluster, as established by Elvidge *et al.* [32]. The two Planck curves represent the two contributors for the IR radiance measured by the sensor at night, i.e. the flaring event and the background, each weighted by its respective relative area:

$$B_\lambda^{obs} \stackrel{!}{=} B(\lambda, T_{bg}) \times \left(1 - \frac{A_{GF}}{A_{cluster}}\right) + B(\lambda, T_{GF}) \times \frac{A_{GF}}{A_{cluster}} \quad (10)$$

$$B(\lambda, T) = \frac{2hc^2}{\lambda^5} \frac{1}{e^{\frac{hc}{\lambda kT}} - 1} \quad (11)$$

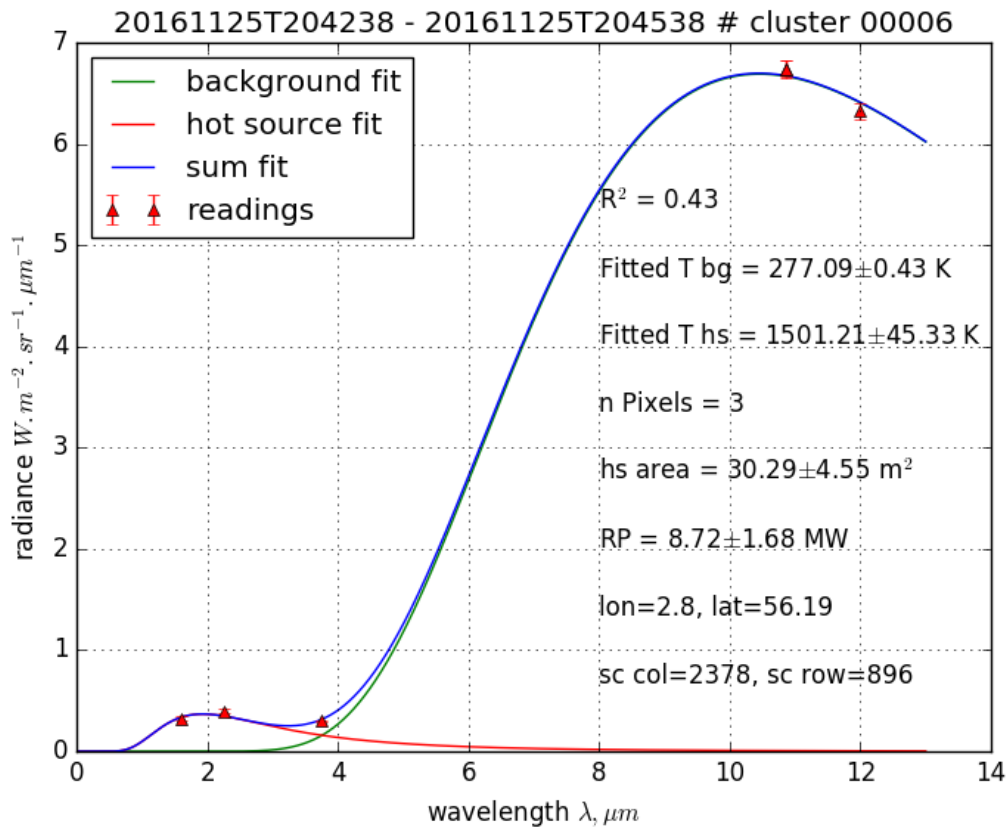


Figure 6. An example of the temperature and area retrieval by dual Planck curve fitting.

where $B(\lambda, T_{GF})$ and $B(\lambda, T_{bg})$ are the modelled gas flare and background radiance, respectively, according to Planck's law. A_{GF} is the modelled flame area [m^2].

The B_{λ}^{obs} values are approximated by fitting the parameters T_{bg} , T_{GF} and A_{GF} via the least squares methodology. The standard deviation of the background radiances σ_{λ}^{bg} is used in the fitting as standard deviation of the cluster radiances. The algorithm computes uncertainties for both the temperature and the area.

3.8. Radiative power

The radiative power (RP) of the hot source may then be computed using the Stefan-Boltzmann equation and assuming a perfect emissivity (in W):

$$RP_{GF} = A_{GF} \times \sigma_{SB} \times T_{GF}^4 \quad (12)$$

where σ_{SB} is the Stefan-Boltzmann constant ($5.670373 \times 10^{-8} W m^{-2} K^{-4}$).

The respective uncertainty is computed by propagation of errors.

4. Results

4.1. Regional study: 4 flaring regions

The described algorithm was applied to observation in the four regions of West Africa, the North sea, the Caspian sea and the Persian gulf, cf. Table 2.

4.1.1. Temperature and area retrievals

Figure 7 shows the hot spot detections of SLSTR with temperatures in the range [500 K, 5000 K], which we consider to be *valid* detections. The methodology successfully captures well-known flaring locations such as the North Sea oil fields, the mouths of the Congo and Niger rivers, the Persian Gulf and the Tigris and Euphrates rivers valleys. However, a large number of hot spots were also detected outside of known flaring regions, e.g. in the North Sea, or in the plateau of central Angola and the Southern D. R. Congo.

Figure 8 shows the temperature distributions in nine specific areas: four areas with known gas flaring, one area with known biomass burning area and four areas without any known gas flaring activity. The retrieved temperatures for the detections in the non-flaring areas is clearly lower than for the flaring areas (see Figure 8). The retrieved temperatures for the biomass burning area is intermediate. Observing fire temperature on a global scale, even only at night-time, is complementary to the widely used burnt area and fire radiative power observations and has great potential for reducing errors in the current fire emission datasets.

Gas flare areas seen from space could be dependent on the viewing angle. However, Figure 9 shows that the retrieved hot spot area is not dependent on the across track index, and therefore the viewing angle.

4.1.2. Persistence

Other hot or bright events that can be observed from space in the IR part of the spectrum at night include wildfires, auroras, industry (e.g. steel mills) and heavily lit boats. Noise and an increased exposition of the sensor to radiation due to the South Atlantic Anomaly may also generate spurious hot spots. [28,32] It is difficult to discriminate between these events based only on the radiance. An analysis of the persistence of the signal at the location of a given valid detection has been proposed to filter out noise and ephemeral phenomena [28,32].

Although not suitable for a thorough analysis due to the short sampling period, the persistent observations (at least 3 detections within a spatial accuracy of ± 0.02 degrees in longitude and latitude over the sampling period) mainly correspond to locations within known flaring regions (see Figure 10). In future works where this methodology will be used on data from longer periods, this threshold might need to be raised or otherwise adapted. For known interferences, persistent or semi-persistent hot sources such as volcanoes, the use of a mask will also be useful.

4.1.3. Selection of persistent observations and radiative power computations

In order to filter low-quality determinations, cloud cover and overfitting were considered.

Clouds may interfere with the amount of radiation measured by the SLSTR instrument, in turn interfering with the temperature, area and radiative power retrievals. However, simply discarding cloudy pixels could incur a large omission error since pixels containing gas flares are frequently marked as clouds, namely as isolated cloudy patches (e.g. for the VIIRS instrument [32]). For this reason, we analyse the cloudiness of the background, as defined in 3.2, and discard only observations with less than 3 cloud-free background pixels.

In order to avoid too much dependence on the TIR channels, which are not subject to the thresholding and clustering process and thus virtually always present, we discard persistent observations for which no S6 or S7/F1 cluster were detected.

Figure 11 shows the distributions of the retrieved temperature, area and radiative power for detections that have been filtered with persistence, cloud cover and S6/S7/F7 availability criteria described above. We will label these "quality persistent" below. The distributions of the quality persistent observations fall within the expected range for gas flares. The retrieved temperatures show a clearly unimodal distribution approximately centered at 1600K for the Persian Gulf and the Caspian Sea test regions. For the North Sea test region, the distribution is bi-modal, with modes around 1000K

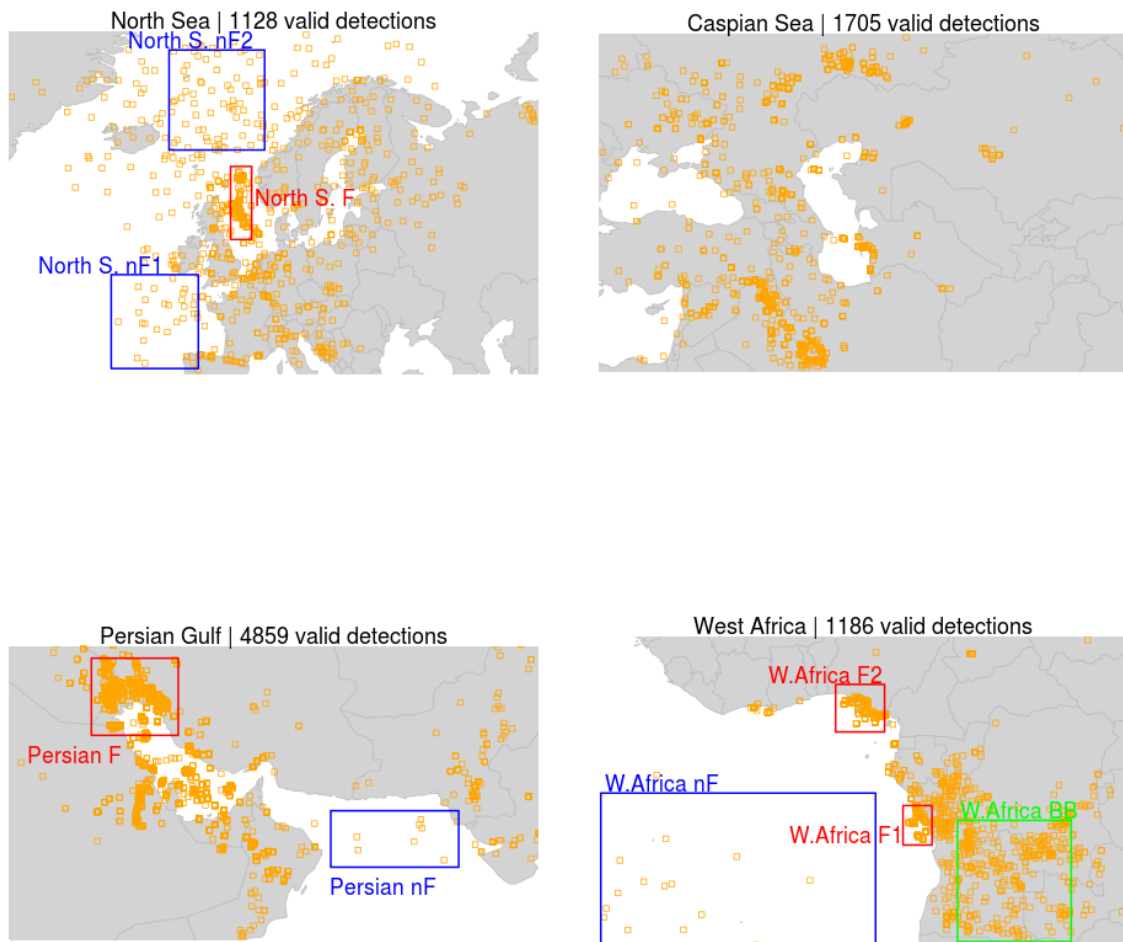


Figure 7. Maps of the valid detections within the test regions. The rectangles represent the 9 study areas (red for flaring, green for biomass burning, blue for non-flaring)

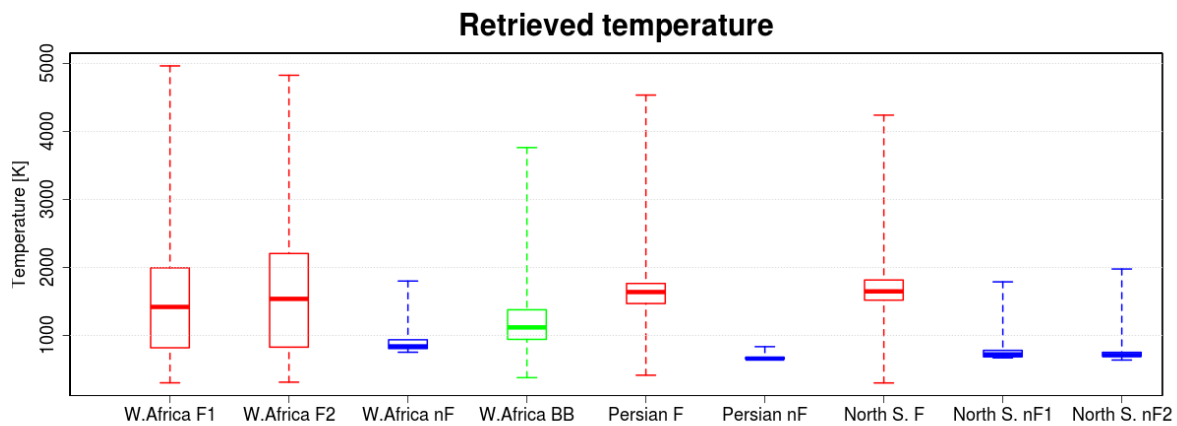


Figure 8. Temperature retrievals distribution for the valid detections within each study area defined in Figure 7.

Table 3. Summary of the detections based on SLSTR and spatial comparison with VIIRS Nightfire.

	N. Sea	C. Sea	P. Gulf	W. Africa
SLSTR				
valid detections	1131	1708	4889	1193
persistent observations	479	1220	4187	394
persistent locations	72	148	359	57
quality persistent observations	203	919	3188	15
persistent locations detected by VIIRS	71	148	359	57

and 1600K. There were very few quality persistent observations for the West Africa test region due to unfavourable cloud conditions.

4.1.4. Comparison with VIIRS Nightfire

The SLSTR valid detections at persistent locations were compared to the VIIRS Nightfire data for a same time period and a roughly similar area. The VIIRS Nightfire results were subject to the same spatial persistency analysis as the SLSTR data (3 times within a spatial accuracy of 0.02 degrees in longitude and latitude). VIIRS detects more gas flaring locations than SLSTR, which can be traced back to its wider swath (3040 km against 1420 km), and thus a shorter revisit time. Another reason for the larger number of detections by VIIRS is that the Nightfire algorithm processes single pixels, selected as the local maxima of pixels above the threshold, the method here aggregates contiguous hot pixels into clusters. Despite these limitations, all but one persistent locations detected by SLSTR were also detected by VIIRS.

The clustering of contiguous hot pixels used in the present method also explains why the VIIRS Nightfire temperature retrievals tend to peak at higher values than the SLSTR ones (Figure 12). Selecting only pixels which are local maxima, as the VIIRS Nightfire algorithm does, will produce detections with higher radiances and mostly higher temperatures will be retrieved.

4.2. Single site study: Bovanenkovo, Yamal peninsula

As another test case, a flaring site in the Bovanenkovo field was observed in more detail. The Bovanenkovo field, located on the western shore of the Yamal peninsula in northern Siberia, Russia, produces natural gas and condensates. The flaring location was repeatedly observed by the sensors SLSTR, HSRS and VIIRS over a sampling period of 19 days (between 15/12/2016 and 2/12/2017),

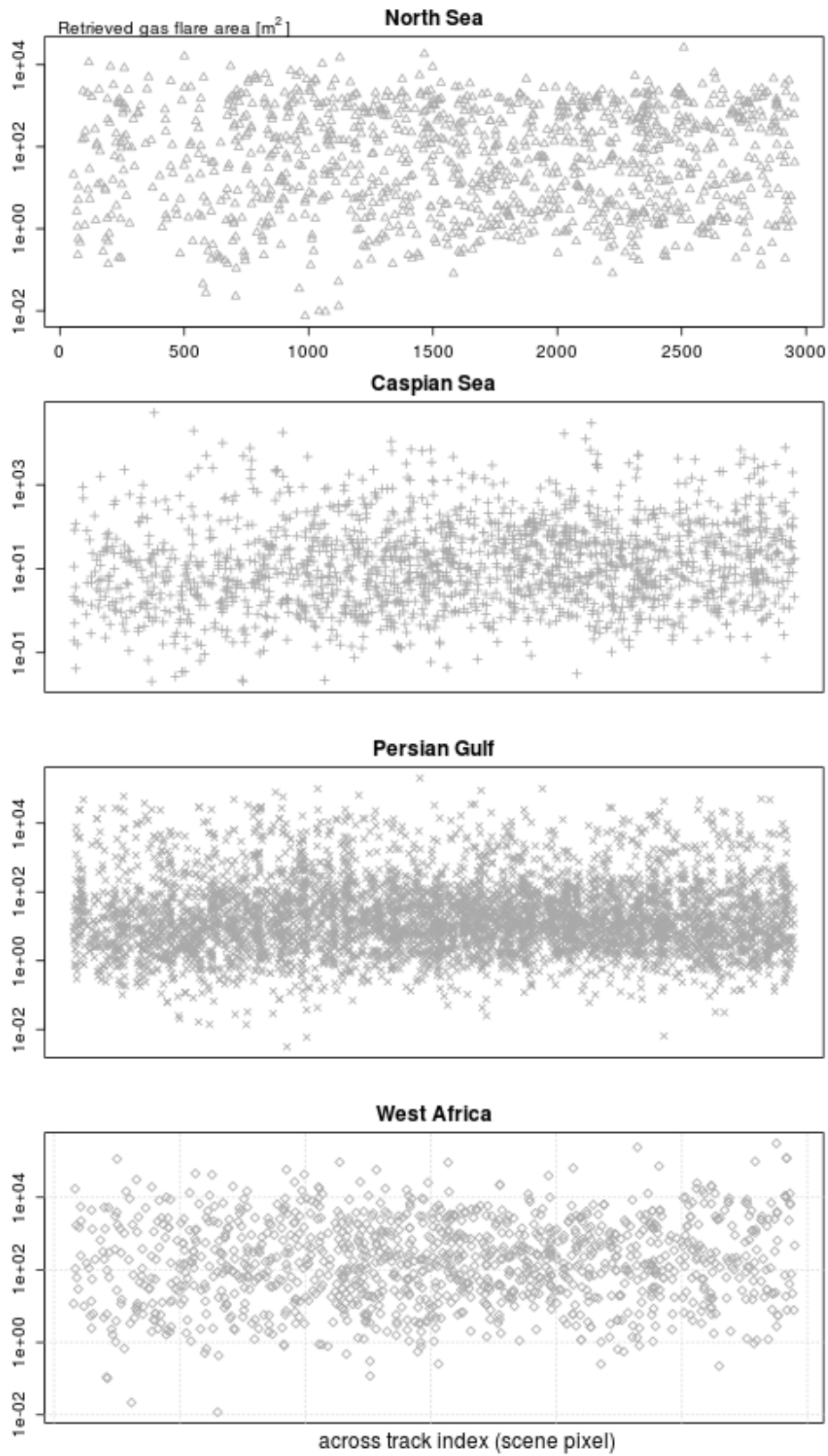


Figure 9. Retrieved gas flare area for valid detections as a function of the across track index.

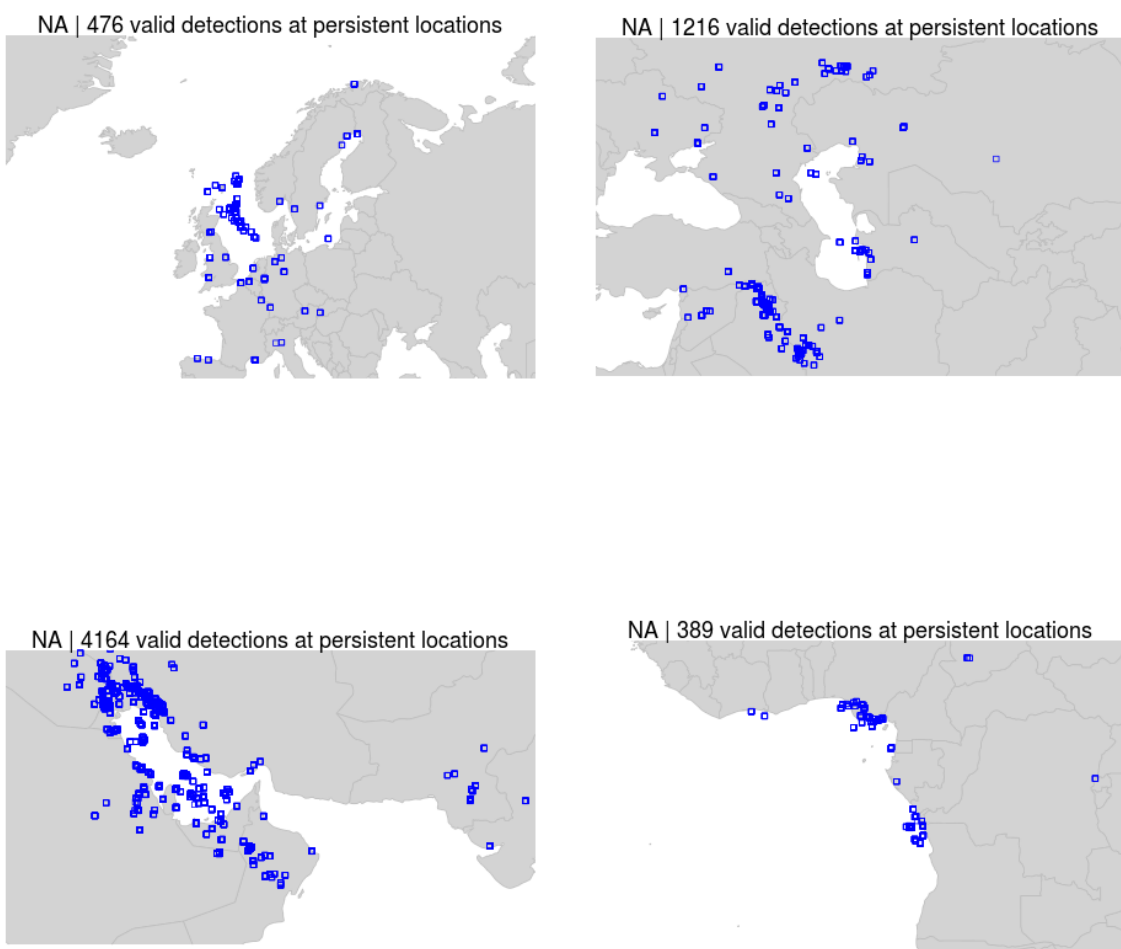


Figure 10. Maps of the persistent observations.

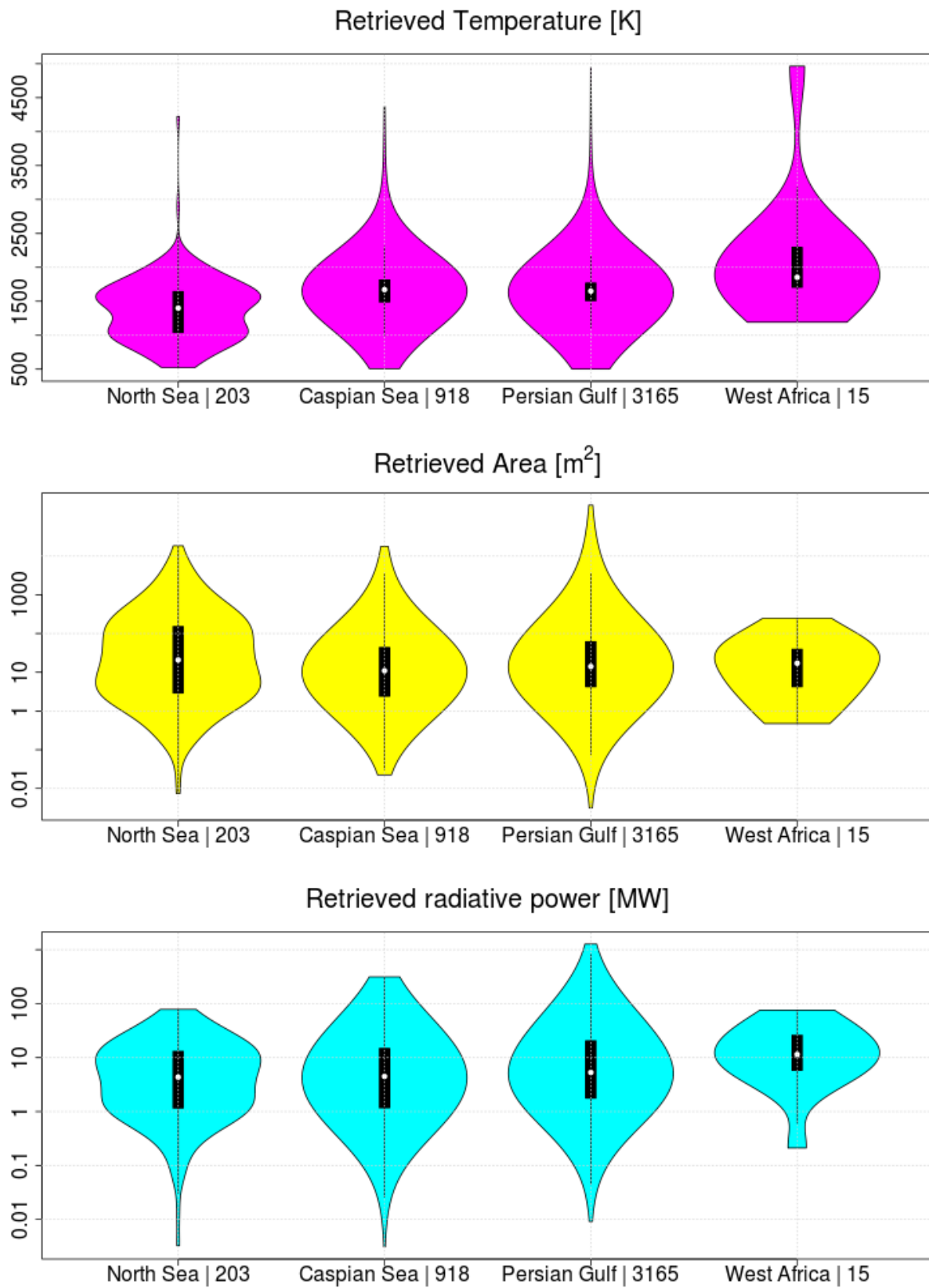


Figure 11. Violin plots for the temperature, area and the radiative power retrieval distributions of the quality persistent observations. The number of quality persistent observations is also indicated.

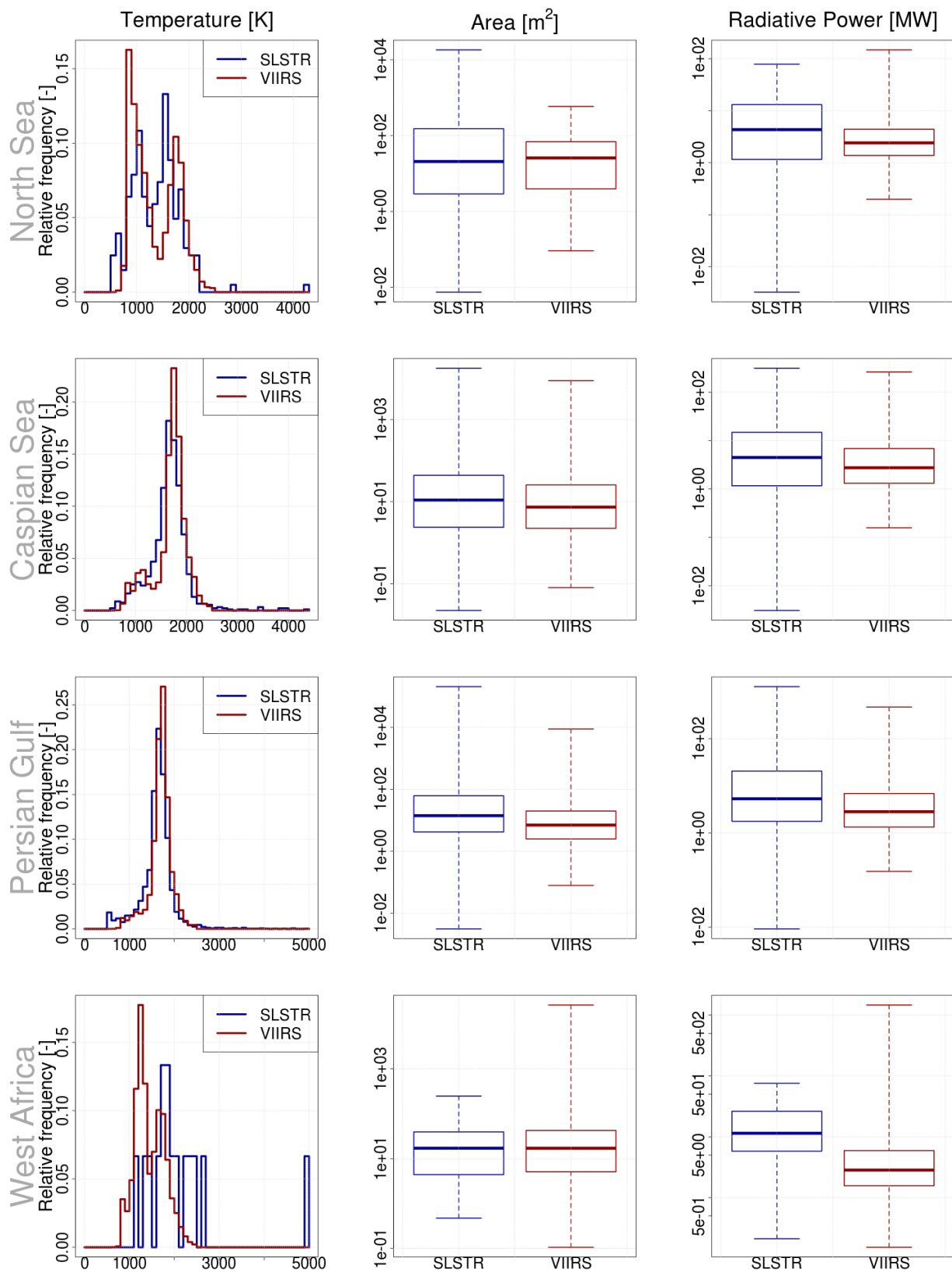


Figure 12. Comparison between temperature, area and radiative power retrieved by SLSTR and VIIRS at persistent locations.

Table 4. Summary of the detections at the Bovanenkovo gas and condensates field in the Yamal Peninsula, Siberia.

	SLSTR	HSRS	VIIRS	Total
Location 1	0	1	0	1
Location 2	1	2	17	20
Location 3	2	3	6	11
Location 4	1	0	0	1
Total	4	6	23	33

with very high temporal co-location between SLSTR and HSRS. The detections are clustered around 4 distinct locations (see Figure 13) and are summarized in Table 4

Due to clustering in the SLSTR and HSRS data analysis, these sensors may detect one cluster in a situation, in which the VIIRS product lists two or more flares in very close proximity. For SLSTR, the observing conditions were very close to twilight (the night-only mask was not considered in order to have the opportunity to observe the same flaring site by the three sensors), and thus not ideal.

Figure 14 shows the temperature, area and radiative power determinations at Locations 2 and 3 for the 3 instruments.

At Location 2, the single SLSTR observation agrees well with the determinations based on VIIRS and HSRS for the temperature. At Location 3, the temperature determinations based on SLSTR are lower than those based on VIIRS but in the same range as those based on HSRS. The gas flare temperature depends on the flared gas composition and the completeness of combustion, which depends on flare design and meteorological conditions [44–47]. Thus the flaring characteristics may vary in time. The methodological differences may also explain lower temperatures in the SLSTR product as explained above. The agreement between SLSTR and HSRS is noteworthy since HSRS uses a bi-spectral method based on the MIR and TIR, the latter of which is prone to low signal/noise ratios for hot spots.

While the retrieved areas from TET-1 are larger than those from SLSTR, area determinations based on VIIRS and SLSTR are close for both locations except the highly uncertain SLSTR observation on 2/1/2017. The shape of the flame, and thus its area as observed by a satellite, is dependent on the flow rate and the meteorological conditions [45,48] and therefore also variable in time as its temperature.

Despite the variability seen between sensors due to inherent variability of flares and methodological differences, the radiative power determinations, the variable to which the emissions computations are linked, compare well between sensors.

5. Conclusions

We have adapted the VIIRS Nightfire algorithm [32] for the detection and characterisation of gas flares using the SLSTR instrument on-board the Copernicus Sentinel-3 satellite [40]. The algorithm is based on fitting Planck curves that represent the hot source and the cool background to all the available satellite observations in the short-wave, mid and thermal infrared spectral range. This approach relies on radiometrically calibrated radiance data as input.

The main difference to the original methodology is that we analyse the integrated radiances of contiguous clusters of hot pixels instead of the maximal radiances detected in the clusters. We expect this representation to be more realistic and accurate for large arrays of gas flares. The presented algorithm furthermore tolerates misregistration and variable footprint areas between different spectral channels. The misregistration itself is quantified in a post-processing step. Finally, a new hot spot detection algorithm is employed and spurious cloud masking of just the hot source is ignored.

The concept of monitoring gas flares with SLSTR using the new algorithm has been tested using Sentinel-3A observations in four regions of interest: North Sea, Caspian Sea, Persian Gulf and Gulf of Guinea.

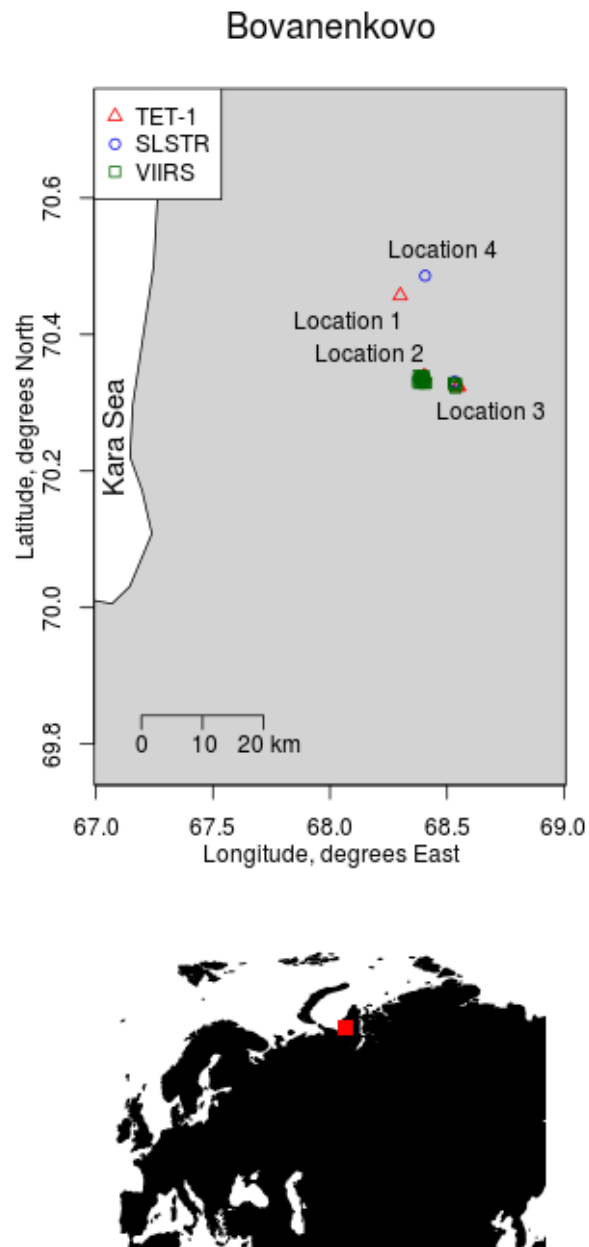


Figure 13. Location of the detections in the Bovanenkovo area between 15/12/2016 and 02/01/2017 (upper) and location of Bovanenkovo in Eurasia (lower).

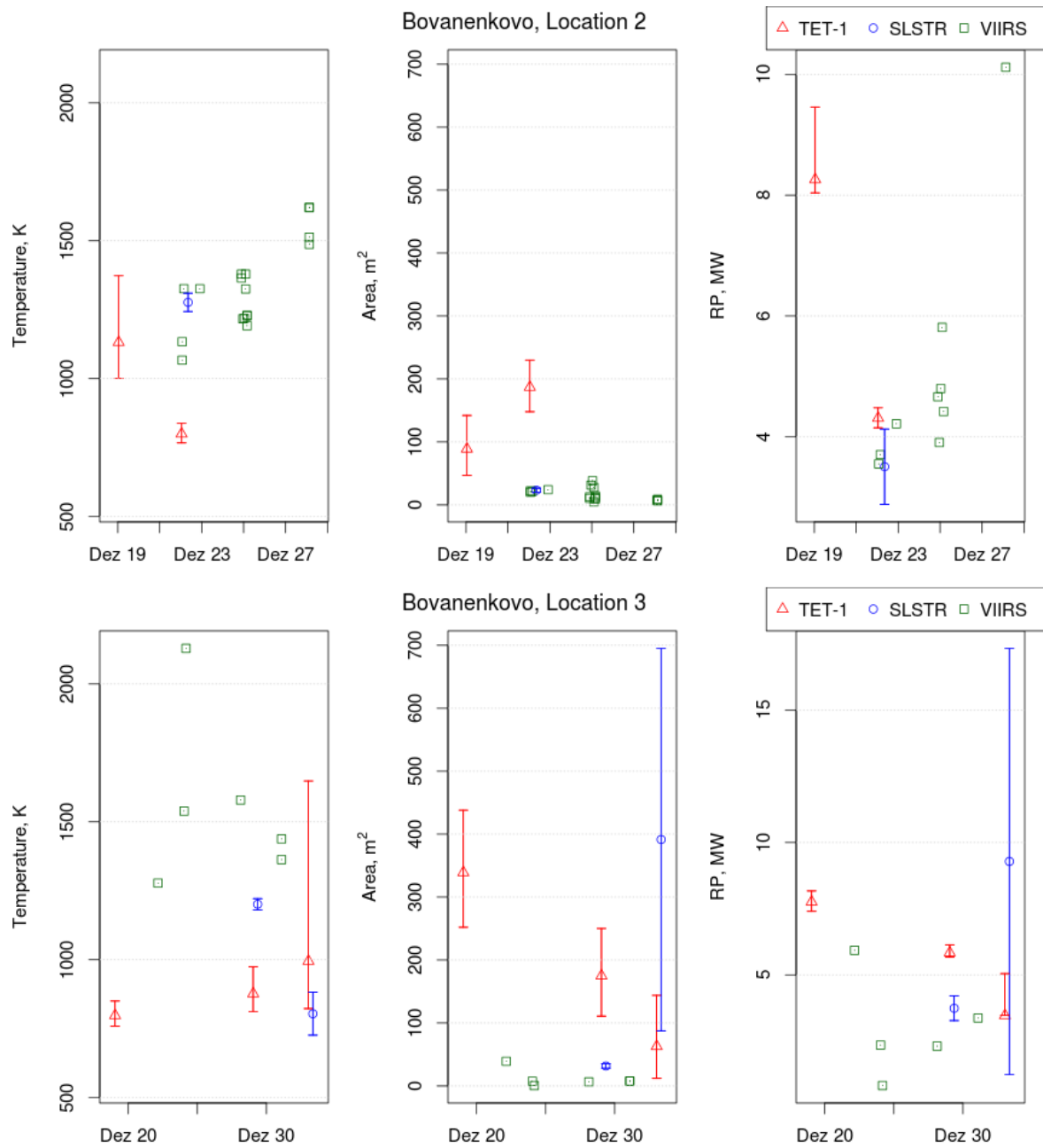


Figure 14. Temperature, area and radiative power determination for the detections at locations 2 and 3. Radiative power determinations based on VIIRS for a same overpass were added.

Our methodology detects gas flaring activity at locations coincident with oil extraction sites and comparisons to the established VIIRS Nightfire product show that the location of the detections is largely consistent. The characterisation of the gas flares in terms of temperature, area and radiative power is also similar. Thus we conclude that night-time gas flaring can be monitored and characterised with the Sentinel-3 satellites. The retrieved gas flare temperatures are slightly lower, areas are slightly larger and radiative power is slightly larger than in the VIIRS Nightfire product. This is expected from the algorithmic difference and thought to more realistically represent large arrays of multiple gas flares.

Our methodology was also tested with a short time series of observations over an individual flaring site at Bovanenkovo on the Yamal peninsula in Siberia. Here, we compare near-coincidental overpasses of Sentinel-3A (SLSTR), TET-1 (HSRS) and Suomi-NPP (VIIRS). In terms of temperature, both SLSTR and HSRS show similar results, while VIIRS retrievals deliver slightly higher temperatures. Areas derived from SLSTR data are similar to those from VIIRS, and smaller than those from HSRS. Taking into consideration the inherent variability of the operation of gas flares, we consider those values, as well as the derived radiative power values, from the three instruments to be in good agreement.

The presented algorithm is suitable for the generation of an operational global gas flaring product from the series of Copernicus Sentinel-3 satellites. Based on the derived FRP of the gas flares, the product may also include estimates of the flared gas volume (BCM) and the emissions of black carbon and other smoke constituents.

Including the gas flaring emissions into the Copernicus Atmosphere Monitoring Service (CAMS) [49,50] will be necessary to simulate realistic black carbon deposition rates in the Arctic and quantify the corresponding albedo reduction and climate effects. This could be achieved by including black carbon emissions from a new Sentinel-3 gas flaring product or by extending the Global Fire Assimilation System (GFAS, [51]) of CAMS to ingest and interpret also FRP from gas flaring as reported by VIIRS Nightfire and a potential future "SLSTR Nightfire" product.

Estimates of the temperatures of vegetation fires are also provided, albeit only at night-time. This is a new observational capability. It is complementary to the burnt area and fire radiative products, which are currently being used for vegetation fire emission estimation, and carries a high potential for reducing some of the large uncertainties in these estimates.

Author Contributions: Conceptualization, Alexandre Caseiro, Johannes W. Kaiser and Gernot Rucker; Methodology, Alexandre Caseiro and Johannes W. Kaiser; Software, Alexandre Caseiro, Joachim Tiemann and David Leimbach; Validation, Alexandre Caseiro, Johannes W. Kaiser, Gernot Rucker, Eckehard Lorenz and Olaf Frauenberger; Formal Analysis, Investigation & Resources, Alexandre Caseiro, Johannes W. Kaiser and Gernot Rucker; Data Curation, Alexandre Caseiro, Gernot Rucker, Eckehard Lorenz and Olaf Frauenberger; Writing—Original Draft Preparation, Alexandre Caseiro; Writing—Review & Editing, Johannes W. Kaiser, Gernot Rucker, Eckehard Lorenz and Olaf Frauenberger; Visualization, Alexandre Caseiro; Supervision, Project Administration & Funding Acquisition, Johannes W. Kaiser.

Funding: This research was funded by the German Federal Ministry for Economic Affairs and Energy (BMW, Bundesministerium für Wirtschaft und Energie) under the contract number FKZ 50EE1339.

Conflicts of Interest: The founding sponsors had no role in the design of the study; in the collection, analyses, or interpretation of data; in the writing of the manuscript, and in the decision to publish the results.

1. Gervet, B. Gas Flaring Emission Contributes to Global Warming. Master's thesis, INSA, Lyon, France and Luleå University of Technology, Luleå, Sweden, 2007.
2. Stohl, A.; Klimont, Z.; Eckhardt, S.; Kupiainen, K.; Shevchenko, V.P.; Kopeikin, V.M.; Novigatsky, A.N. Black carbon in the Arctic: the underestimated role of gas flaring and residential combustion emissions. *Atmospheric Chemistry and Physics* **2013**, *13*, 8833–8855. doi:10.5194/acp-13-8833-2013.
3. Huang, K.; Fu, J.S.; Prikhodko, V.Y.; Storey, J.M.; Romanov, A.; Hodson, E.L.; Cresko, J.; Morozova, I.; Ignatieva, Y.; Cabaniss, J. Russian anthropogenic black carbon: Emission reconstruction and Arctic black

- carbon simulation. *Journal of Geophysical Research: Atmospheres* **2015**, *120*, 11,306–11,333. 2015JD023358, doi:10.1002/2015JD023358.
4. Quinn, P.K.; Shaw, G.; Andrews, E.; Dutton, E.G.; Ruoho Airola, T.; Gong, S.L. Arctic haze: current trends and knowledge gaps. *Tellus B* **2007**, *59*, 99–114. doi:10.1111/j.1600-0889.2006.00238.x.
 5. Doherty, S.J.; Warren, S.G.; Grenfell, T.C.; Clarke, A.D.; Brandt, R.E. Light-absorbing impurities in Arctic snow. *Atmospheric Chemistry and Physics* **2010**, *10*, 11647–11680. doi:10.5194/acp-10-11647-2010.
 6. Serreze, M.C.; Barry, R.G. Processes and impacts of Arctic amplification: A research synthesis. *Global and Planetary Change* **2011**, *77*, 85 – 96. doi:https://doi.org/10.1016/j.gloplacha.2011.03.004.
 7. Walsh, J.E. Intensified warming of the Arctic: Causes and impacts on middle latitudes. *Global and Planetary Change* **2014**, *117*, 52 – 63. doi:https://doi.org/10.1016/j.gloplacha.2014.03.003.
 8. Li, C.; Hsu, N.C.; Sayer, A.M.; Krotkov, N.A.; Fu, J.S.; Lamsal, L.N.; Lee, J.; Tsay, S.C. Satellite observation of pollutant emissions from gas flaring activities near the Arctic. *Atmospheric Environment* **2016**, *133*, 1 – 11. doi:http://dx.doi.org/10.1016/j.atmosenv.2016.03.019.
 9. Ismail, O.; Umukoro, G. Global Impact of Gas Flaring. *Energy and Power Engineering* **2012**, *4*, 290 – 302. doi:10.4236/epe.2012.44039.
 10. Aghalino, S.O. Gas Flaring, Environmental Pollution and Abatement Measures in Nigeria, 1969 – 2001. *Journal of sustainable development in Africa* **2009**, *11*, 219–238.
 11. Nwoye, C.I.; Nwakpa, S.O.; Nwosu, I.E.; Odo, J.U.; Chinwuko, E.C.; Idenyi, N.E. Multi-Factorial Analysis of Atmospheric Noise Pollution Level Based on Emitted Carbon and Heat Radiation during Gas Flaring. *Journal of Atmospheric Pollution* **2014**, *2*, 22–29. doi:10.12691/jap-2-1-5.
 12. Anomohanran, O. Determination of greenhouse gas emission resulting from gas flaring activities in Nigeria. *Energy Policy* **2012**, *45*, 666 – 670. doi:http://dx.doi.org/10.1016/j.enpol.2012.03.018.
 13. Ajao, E.A.; Anurigwo, S. Land-Based Sources of Pollution in the Niger Delta, Nigeria. *Ambio* **2002**, *13*, 442–445.
 14. Julius, O.O. Environmental impact of gas flaring within Umutu-Ebedei gas plant in Delta State, Nigeria. *Archives of Applied Science Research* **2011**, *3*, 272–279.
 15. Obioh, I.; Oluwole, A.F.; Akeredolu, F.A. Non-CO₂ gaseous emissions from upstream oil and gas operations in Nigeria. *Environmental Monitoring and Assessment* **1994**, *31*, 67–72.
 16. Uzomah, V.; Sangodoyin, A. Rainwater chemistry as influenced by atmospheric deposition of pollutants in Southern Nigeria. *Environmental Management and Health* **2000**, *11*, 149–156, [https://doi.org/10.1108/09566160010321569]. doi:10.1108/09566160010321569.
 17. Nwaichi, E.; Uzazobona, M. Estimation of the CO₂ Level due to Gas Flaring in the Niger Delta. *Research Journal of Environmental Sciences* **2011**, *5*, 565–572. doi:10.3923/rjes.2011.565.572.
 18. Onu, P.u.; Quan, X.; Ling, X. Acid rain: an analysis on the cause, impacts and abatement measures Niger Delta perspective, Nigeria. *International Journal of Scientific & Engineering Research* **2014**, *5*, 1214–1219.
 19. Croft, T. Burning waste gas in oil fields. *Nature* **1973**, *245*, 375–376.
 20. Croft, T. Nighttime images of the earth from space. *Scientific American* **1978**, *239*, 86–98. doi:10.1038/scientificamerican0778-86.
 21. Elvidge, C.D.; Imhoff, M.L.; Baugh, K.E.; Hobson, V.R.; Nelson, I.; Safran, J.; Dietz, J.B.; Tuttle, B.T. Night-time lights of the world: 1994, 1995. *[ISPRS] Journal of Photogrammetry and Remote Sensing* **2001**, *56*, 81 – 99. doi:http://dx.doi.org/10.1016/S0924-2716(01)00040-5.
 22. Elvidge, C.D.; Baugh, K.E.; Tuttle, B.T.; Howard, A.T.; Pack, D.W.; Milesi, C.; Erwin, E.H. A Twelve Year Record of National and Global Gas Flaring Volumes Estimated Using Satellite Data. Technical report, World Bank, 2007.
 23. Elvidge, C.D.; Ziskin, D.; Baugh, K.E.; Tuttle, B.T.; Ghosh, T.; Pack, D.W.; Erwin, E.H.; Zhizhin, M. A Fifteen Year Record of Global Natural Gas Flaring Derived from Satellite Data. *Energies* **2009**, *2*, 595–622. doi:10.3390/en20300595.
 24. Mota, B.W.; Pereira, J.M.C.; Oom, D.; Vasconcelos, M.J.P.; Schultz, M. Screening the ESA ATSR-2 World Fire Atlas (1997–2002). *Atmospheric Chemistry and Physics* **2006**, *6*, 1409–1424. doi:10.5194/acp-6-1409-2006.
 25. Oom, D.; Pereira, J. Exploratory spatial data analysis of global {MODIS} active fire data. *International Journal of Applied Earth Observation and Geoinformation* **2013**, *21*, 326 – 340. doi:http://dx.doi.org/10.1016/j.jag.2012.07.018.

26. Elvidge, C.D.; Baugh, K.E.; Ziskin, D.; Anderson, S.; Ghosh, T. Estimation of Gas Flaring Volumes Using NASA MODIS Fire Detection Products. Technical report, NOAA National Geophysical Data Center, 2011.
27. Faruolo, M.; Coviello, I.; Filizzola, C.; Lacava, T.; Pergola, N.; Tramutoli, V. A satellite-based analysis of the Val d'Agri Oil Center (southern Italy) gas flaring emissions. *Natural Hazards and Earth System Science* **2014**, *14*, 2783–2793. doi:10.5194/nhess-14-2783-2014.
28. Casadio, S.; Arino, O.; Serpe, D. Gas flaring monitoring from space using the {ATSR} instrument series. *Remote Sensing of Environment* **2012**, *116*, 239 – 249. Advanced Along Track Scanning Radiometer(AATSR) Special Issue, doi:http://dx.doi.org/10.1016/j.rse.2010.11.022.
29. Casadio, S.; Arino, O.; Minchella, A. Use of {ATSR} and {SAR} measurements for the monitoring and characterisation of night-time gas flaring from off-shore platforms: The North Sea test case. *Remote Sensing of Environment* **2012**, *123*, 175 – 186. doi:http://dx.doi.org/10.1016/j.rse.2012.03.021.
30. Elvidge, C.D.; Zhizhin, M.; Hsu, F.C.; Baugh, K.E. VIIRS Nightfire: Satellite Pyrometry at Night. *Remote Sensing* **2013**, *5*, 4423–4449. doi:10.3390/rs5094423.
31. Anejionu, O.C.D.; Blackburn, G.A.; Whyatt, J.D. Satellite survey of gas flares: development and application of a Landsat-based technique in the Niger Delta. *International Journal of Remote Sensing* **2014**, *35*, 1900–1925, [<http://dx.doi.org/10.1080/01431161.2013.879351>]. doi:10.1080/01431161.2013.879351.
32. Elvidge, C.D.; Zhizhin, M.; Baugh, K.; Hsu, F.C.; Ghosh, T. Methods for Global Survey of Natural Gas Flaring from Visible Infrared Imaging Radiometer Suite Data. *Energies* **2016**, *9*, 14. doi:10.3390/en9010014.
33. Dozier, J. A Method for Satellite Identification of Surface Temperature Fields of Subpixel Resolution. *Remote Sensing of the Environment* **1981**, *11*, 221–119.
34. Brieß, K.; Bärwald, W.; Gill, E.; Kayal, H.; Montenbruck, O.; Montenegro, S.; Halle, W.; Skrbek, W.; Studemund, H.; Terzibaschian, T.; Venus, H. Technology demonstration by the BIRD-mission. *Acta Astronautica* **2005**, *56*, 57 – 63. 4th {IAA} International Symposium on Small Satellites for Earth Observation, doi:http://dx.doi.org/10.1016/j.actaastro.2004.09.041.
35. Walter, I.; Briess, K.; Baerwald, W.; Lorenz, E.; Skrbek, W.; Schrandt, F. A microsatellite platform for hot spot dedection. *Acta Astronautica* **2005**, *56*, 221 – 229. 4th {IAA} International Symposium on Small Satellites for Earth Observation, doi:http://dx.doi.org/10.1016/j.actaastro.2004.09.009.
36. Zhukov, B.; Lorenz, E.; Oertel, D.; Wooster, M.; Roberts, G. Spaceborne detection and characterization of fires during the bi-spectral infrared detection (BIRD) experimental small satellite mission (2001–2004). *Remote Sensing of Environment* **2006**, *100*, 29 – 51. doi:http://dx.doi.org/10.1016/j.rse.2005.09.019.
37. Oertel, D.; Briess, K.; Lorenz, E.; Skrbek, W.; Zhukov, B. Detection, monitoring and quantitative analysis of wildfires with the BIRD satellite. Remote Sensing for Agriculture, Ecosystems, and Hydrology V; Owe, M.; D'Urso, G.; Moreno, J.F.; Calera, A., Eds.; SPIE, SPIE Bellingham, WA: Remote Sensing for Agriculture, Ecosystems, and Hydrology V, 8 - 12 September 2003, Barcelona, Spain, 2004; Vol. 5232, *Proceedings of SPIE*, pp. 208–218. doi:10.1117/12.511051.
38. Zhukov, B.; Briess, K.; Lorenz, E.; Oertel, D.; Skrbek, W. Detection and analysis of high-temperature events in the {BIRD} mission. *Acta Astronautica* **2005**, *56*, 65 – 71. 4th {IAA} International Symposium on Small Satellites for Earth Observation, doi:http://dx.doi.org/10.1016/j.actaastro.2004.09.014.
39. Reile, H.; Lorenz, E.; Terzibaschian, T. The FireBird mission-a scientific mission for Earth observation and hot spot detection. DLR, 2013.
40. Coppo, P.; Ricciarelli, B.; Brandani, F.; Delderfield, J.; Ferlet, M.; Mutlow, C.; Munro, G.; Nightingale, T.; Smith, D.; Bianchi, S.; Nicol, P.; Kirschstein, S.; Hennig, T.; Engel, W.; Frerick, J.; Nieke, J. SLSTR: a high accuracy dual scan temperature radiometer for sea and land surface monitoring from space. *Journal of Modern Optics* **2010**, *57*, 1815–1830, [<https://doi.org/10.1080/09500340.2010.503010>]. doi:10.1080/09500340.2010.503010.
41. Anejionu, O.C.; Blackburn, G.A.; Whyatt, J.D. Detecting gas flares and estimating flaring volumes at individual flow stations using {MODIS} data. *Remote Sensing of Environment* **2015**, *158*, 81 – 94. doi:http://dx.doi.org/10.1016/j.rse.2014.11.018.
42. Muirhead, K.; Cracknell, A.P. Identification of gas flares in the North Sea using satellite data. *International Journal of Remote Sensing* **1984**, *5*, 199–212, [<http://dx.doi.org/10.1080/01431168408948798>]. doi:10.1080/01431168408948798.
43. Smith, D. Sentinel-3 SLSTR – Performance and Calibration. Sentinel-3 Validation Team Meeting. EUMETSAT, 2018.

44. Johnson, M.; Kostiuk, L. Efficiencies of low-momentum jet diffusion flames in crosswinds. *Combustion and Flame* **2000**, *123*. doi:10.1016/s0010-2180(00)00151-6.
45. Leahey, D.; Preston, K.; Stroscher, M. Theoretical and observational assessments of flare efficiencies. *J Air Waste Manag Assoc.* **2001**, *51*, 1610–1616.
46. Johnson, M.; Kostiuk, L. A parametric model for the efficiency of a flare in crosswind. *Proceedings of the Combustion Institute* **2002**, *29*, 1943 – 1950. doi:http://dx.doi.org/10.1016/S1540-7489(02)80236-X.
47. Ismail, O.S.; Umukoro, G.E. Modelling combustion reactions for gas flaring and its resulting emissions. *Journal of King Saud University - Engineering Sciences* **2016**, *28*, 130 – 140. doi:https://doi.org/10.1016/j.jksues.2014.02.003.
48. Pohl, J.H.; Tichenor, B.A.; Lee, J.; Payne, R. Combustion Efficiency of Flares. *Combustion Science and Technology* **1986**, *50*, 217–231, [<http://dx.doi.org/10.1080/00102208608923934>]. doi:10.1080/00102208608923934.
49. Hollingsworth, A.; Engelen, R.J.; Benedetti, A.; Dethof, A.; Flemming, J.; Kaiser, J.W.; Morcrette, J.J.; Simmons, A.J.; Textor, C.; Boucher, O.; Chevallier, F.; Rayner, P.; Elbern, H.; Eskes, H.; Granier, C.; Peuch, V.H.; Rouil, L.; Schultz, M.G. Toward a Monitoring and Forecasting System For Atmospheric Composition: The GEMS Project. *Bulletin of the American Meteorological Society* **2008**, *89*, 1147–1164, [<https://doi.org/10.1175/2008BAMS2355.1>]. doi:10.1175/2008BAMS2355.1.
50. Stein, O.; Flemming, J.; Inness, A.; Kaiser, J.W.; Schultz, M.G. Global reactive gases forecasts and reanalysis in the MACC project. *Journal of Integrative Environmental Sciences* **2012**, *9*, 57–70, [<https://doi.org/10.1080/1943815X.2012.696545>]. doi:10.1080/1943815X.2012.696545.
51. Kaiser, J.W.; Heil, A.; Andreae, M.O.; Benedetti, A.; Chubarova, N.; Jones, L.; Morcrette, J.J.; Razinger, M.; Schultz, M.G.; Suttie, M.; van der Werf, G.R. Biomass burning emissions estimated with a global fire assimilation system based on observed fire radiative power. *Biogeosciences* **2012**, *9*, 527–554. doi:10.5194/bg-9-527-2012.